Jour. of the KGS, Vol. 22, No. 9. September 2006, pp. 45~59

Implicit Numerical Integration of Two-surface Plasticity Model for Coarse-grained Soils

Implicit 수치적분 방법을 이용한 조립토에 관한 구성방정식의 수행

Choi, Changho[1] 최 창 호

요 지

탄소성 구성방정식은 주로 미분방적식(rate equation) 으로 이루어져 있기 때문에 유한요소법 등을 이용한 지반구조물 해석시 미분방정식들에 대한 수치적분을 수행할수 있는 방법이 필요하다. 구조물의 거동을 해석할시 미분방정식들을 위한 적분방법은 해석결과의 정확성과 유한요소법 모델링의 안전성에 큰 영향을 미치고 있다. 본 논문에서는 최근에 개발되어 사용되고 있는 흙에 관한 구성모델인 "Two-surface soil plasticity model (Manzari and Dafalias 1997)"을 Implicit return-mapping 수치적분방법을 이용하여 실행하는 과정을 제시한다. 본 연구에서 사용된 수치적분방법은 Closest-Point-Projection Method(CPPM) 방법으로 탄성 예측자-소성 교정자(elastic predictor-plastic corrector) 개념을 Implicit Backward Euler방법으로 체계화 시킨 알고리듬이다. 본 연구에서 수행한 "Two-surface soil plasticity model"은 조립토의 비선형거동을 해석하며, Bounding surface 개념 및 비선형 등방경화와 이동경화 법칙을 사용하는 모델이다. 본 연구는 CPPM 방법이 정확하고 안정되며 유용한 수치적분을 수행할 수 있는 알고리듬이라는 것을 제시한다. 또한, CPPM 알고리듬은 구성방정식의 해를 반복적으로 해석하는 동안 "Consistent tangent operator $d\sigma/d\varepsilon$"를 제공하므로, 비선형 유한요소 해석이 2차(quadratic convergence rate)의 수렴 조건을 만족하는데 기여한다는 것을 보여준다.

Abstract

The successful performance of any numerical geotechnical simulation depends on the accuracy and efficiency of the numerical implementation of constitutive model used to simulate the stress-strain (constitutive) response of the soil. The corner stone of the numerical implementation of constitutive models is the numerical integration of the incremental form of soil-plasticity constitutive equations over a discrete sequence of time steps. In this paper a well known two-surface soil plasticity model is implemented using a generalized implicit return mapping algorithm to arbitrary convex yield surfaces referred to as the Closest-Point-Projection method (CPPM). The two-surface model describes the nonlinear behavior of coarse-grained materials by incorporating a bounding surface concept together with isotropic and kinematic hardening as well as fabric formulation to account for the effect of fabric formation on the unloading response. In the course of investigating the performance of the CPPM integration method, it is proven that the algorithm is an accurate, robust, and efficient integration technique useful in finite element contexts. It is also shown that the algorithm produces a consistent tangent operator $\frac{d\sigma}{d\varepsilon}$ during the iterative process with quadratic convergence rate of the global iteration process.

Keywords : Closest-Point-Projection method, Constitutive model, Implicit integration, Return mapping, coarse-grained soil

1 Member, Post-Doc., Geotechnical Engineering Research Dept., Korea Institute of Construction Technology, chchoi@kict.re.kr

1. Introduction

There has been increased use of numerical analysis in geotechnical engineering in both research and practice. Among all possible numerical schemes, the finite element analysis has proven to be an efficient method for the analysis of geotechnical applications. Recently, the wide use of the finite element analysis has led the demand on efficient and robust implementations of constitutive equations. The corner stone of the numerical implementation of constitutive models is the numerical integration of the incremental form of soil-plasticity constitutive equations over a discrete sequence of time steps. In the context of finite elements, the integration of discretized constitutive relations is commonly carried out over Gauss quadrature points where the evolution of the initial boundary value problem that defines the inelastic material behavior is enforced locally as a system of differential equations. As a consequence, three factors have a significant effect on the accuracy, cost, and convergence rate of global finite element solutions: a) precision with which the constitutive relations are integrated, b) efficiency of the algorithm, and c) structure of the constitutive stiffness matrix.

The most widely-used integration schemes for the solution of constitutive rate equations fall within the category of elastic predictor-plastic corrector methods (Ortiz et al. 1983), where a purely elastic trial state is followed by a plastic corrector stage (return mapping algorithm). The purpose of the latter is to enforce consistency at the end of the time step in a manner consistent with a prescribed loading function and flow rule. For simple classical plasticity models, such as J2-plasticity, the return path can be determined in closed-form. For complex models that account for pressure sensitive, non-linear work hardening/softening, non-linear elasticity, or complicated yield surfaces, it becomes necessary to compute the return path in an iterative fashion.

Return mapping algorithms are further grouped into explicit and implicit schemes depending on the method used to evaluate the unknown variables in a discrete time space. The former involves only function evaluations and no system of equations needs to be solved to update the state of the material. The cutting plane method, originally proposed by Ortiz and Simo (1986), falls within this class. The main drawback of explicit methods is that relatively large time steps deteriorate the numerical stability. However, the lack of need for an iterative scheme is an attractive factor (Simo 1998; Simo and Hughes 1998). On the contrary, implicit methods are more stable but require the solution of systems of nonlinear equations usually through iterative processes. These methods are commonly used in cases where large time steps are expected. The generalized implicit return mapping algorithm to arbitrary convex yield surfaces was introduced by Simo and Taylor (1986) and Simo and Hughes (1987) and since then has been referred to as the Closest-Point-Projection method (CPPM). The CPPM boils down to the systematic application of Newton's method to a system of nonlinear equations to compute the closest-point projection from a trial state onto a convex yield surface. The fact that it provides an exact linearization of the algorithm leading to the notion of the algorithmic elastoplastic consistent moduli, together with its robustness from an implicit point of view, have motivated a number of recent studies (Borja and Lee 1990; Borja 1991; Hashash and Whittle 1992; Jeremic and Sture 1997; Macari et al. 1997; Borja et al. 2001; Manzari and Prachathananukit (2001); Jacobsson and Runesson 2002).

The objective of this paper is to implement a well known two-surface soil plasticity model in the context of the Closest-Point-Projection method. The two-surface model describes nonlinear elastic behavior of granular materials by incorporating a hypo-elastic formulation at which a direct incremental stress-strain relation using power series is assumed. To account for irreversible response, the critical state two-surface plasticity model was formulated based on classical plasticity theory for cohesionless soils and includes an associative flow rule for the deviatoric component and a nonassociative flow rule for the volumetric part. The model includes isotropic and kinematic hardening as well as fabric formulation to account for the effect of fabric formation on unloading responses. It has a capability to reproduce complex soil behavior subjected to cyclic loading condition.

Table 1. Representation of stress and strain

Stress Representation	Strain Representation	Other Notations
$\sigma_{ij}=\begin{bmatrix}\sigma_1 & 0 & 0\\ 0 & \sigma_2 & 0\\ 0 & 0 & \sigma_3\end{bmatrix}$	$\varepsilon_{ij}=\begin{bmatrix}\varepsilon_1 & 0 & 0\\ 0 & \varepsilon_2 & 0\\ 0 & 0 & \varepsilon_3\end{bmatrix}$	Δu: pore water pressure increment
$p=\frac{1}{3}(\sigma_1+\sigma_2+\sigma_3)$	$\varepsilon_v=\varepsilon_1+\varepsilon_2+\varepsilon_3$	
$s_{ij}=\begin{bmatrix}\sigma_1-p & 0 & 0\\ 0 & \sigma_2-p & 0\\ 0 & 0 & \sigma_3-p\end{bmatrix}$	$e_{ij}=\begin{bmatrix}\varepsilon_1-\varepsilon_v/3 & 0 & 0\\ 0 & \varepsilon_1-\varepsilon_v/3 & 0\\ 0 & 0 & \varepsilon_1-\varepsilon_v/3\end{bmatrix}$	
$J_2=\frac{1}{2}\left(s_1^2+s_2^2+s_3^2\right)$		
$J_3=s_1s_2s_3$	$J'_2=\frac{1}{2}\left(e_1^2+e_2^2+e_3^2\right)$	
$\theta=\frac{1}{3}\cos^{-1}\left(\frac{3\sqrt{3}}{3}\frac{J_3}{J_2^{1/2}}\right)$	$\varepsilon_s=\sqrt{\frac{4}{3}J'_2}$	
$q=\sqrt{3J_2}$		

The following sections introduce the two-surface soil plasticity model proposed by Manzari-Dafalias (1997) and the implementation of the model using return mapping algorithm (Closest-Point-Projection method). Then, in order to investigate performance of the model within CPPM integration method, model simulations of stress-strain behavior for coarse-grained soils subjected to realistic stress paths encountered in soil testing are presented. The accuracy and efficiency of the integration technique in finite element context are also investigated.

In the following, the compressive stress and strain are positive and boldface are used to denote tensors. The representations of stress and strain tensors are summarized in Table 1.

2. Brief Description of the Manzari-Dafalias Two-surface Soil Model

The model formulation proposed by Manzari and Dafalias (1997) combines the concept of bounding surface, where the evolution of plastic modulus is obtained based on the distance from the current state to an image state in the bounding surface, and the influence of the state parameter $\psi=e-e_{cs}$ on the volumetric response within critical state concepts for cohesionless soils, where e and e_{cs} are the void ratio and the critical void ratio, respectively. The bounding surface formulation takes place in a deviatoric stress-ratio space and the state parameter ψ is used to define the volumetric response of cohesionless soils. A distinct feature of the model is its capabilities to describe hardening and softening response based on its state and drainage condition. Moreover, using a single set of model parameters the model captures the response of granular materials with different void ratios and confining pressures. More details of the model can be found in Manzari and Dafalias (1997), Manzari and Prachathananukit (2001), and Choi (2004). A brief description on the model follows.

2.1 Yield Criteria in 3-D Stress Space and Flow Rule

The yield surface is expressed in stress space by a direct generalization of the wedge-type shape. Using a circular cone shape, with apex at the origin, the following expression results

$$f(\boldsymbol{\sigma},\boldsymbol{\alpha},m)=\|\mathbf{r}\|-\sqrt{\frac{2}{3}}mp \tag{1}$$

where,

$$\mathbf{r} = \mathbf{s} - p\boldsymbol{\alpha} \tag{2}$$

$$\|\mathbf{r}\| = \sqrt{\mathbf{r} : \mathbf{r}} \tag{3}$$

and the deviatoric back-stress ratio tensor α and stress ratio scalar m describe the kinematic and the isotropic evolution of the yield surface, respectively. Its projection onto a deviatoric stress ratio, s_i / p where $i = 1,2,3$, plane is a circular-like shape as shown in Fig. 1. The yield function represented by Eqn. 1 plots as a circular cone centered at α with radius of $\sqrt{\frac{2}{3}}m$ and apex at the origin

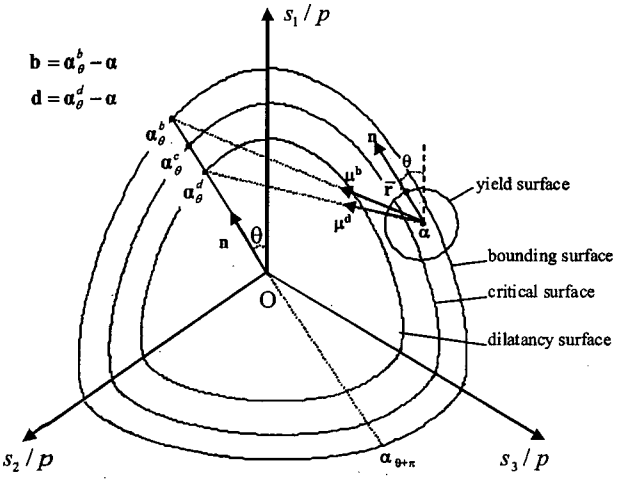

Fig. 1. Schematic illustration of yield, bounding, critical, and dilatancy surfaces in stress-ratio deviatoric plane, and 'image' back-stress ratios $\boldsymbol{\alpha}_\theta^b$, $\boldsymbol{\alpha}_\theta^c$, and $\boldsymbol{\alpha}_\theta^d$ as related to $\boldsymbol{\alpha}$, $\mathbf{n}$, and Lode angle θ (after Manzari and Dafalias, 1997).

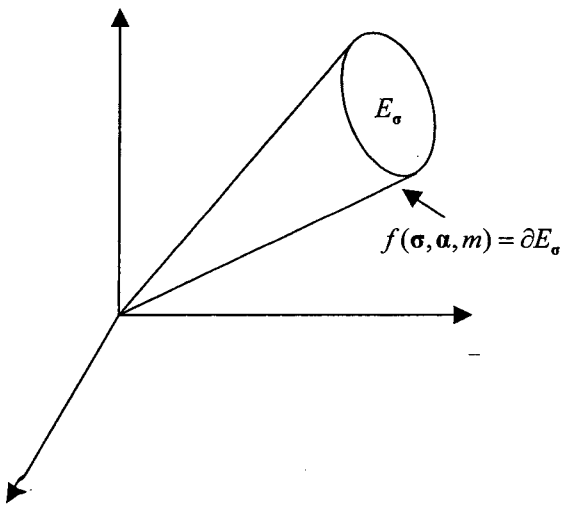

Fig. 2. Schematic view of circular yield surface in three dimensional principal stress space.

as shown in Fig. 2. Plastically admissible stress states, σ, are restrained to a convex set defined by

$$E_\sigma := \{(\boldsymbol{\sigma}, \boldsymbol{\alpha}, m) \in \mathbf{S} \times \mathbf{R}^m | f(\boldsymbol{\sigma}, \boldsymbol{\alpha}, m) \le 0\} \tag{4}$$

By denoting $E_\sigma := \text{int}(E_\sigma) \cup \partial E_\sigma$, the pure elastic domain $\text{int}(E_\sigma)$ and the elastic boundary ∂E_σ are given by

$$\text{int}(E_\sigma) := \{(\boldsymbol{\sigma}, \boldsymbol{\alpha}, m) \in \mathbf{S} \times \mathbf{R}^m | f(\boldsymbol{\sigma}, \boldsymbol{\alpha}, m) < 0\} \tag{5}$$

$$\partial E_\sigma := \{(\boldsymbol{\sigma}, \boldsymbol{\alpha}, m) \in \mathbf{S} \times \mathbf{R}^m | f(\boldsymbol{\sigma}, \boldsymbol{\alpha}, m) = 0\} \tag{6}$$

Since Eqn. 1 defines an open elastic set along the hydrostatic axis, it implies that pure volumetric yielding does not occur.

The normal to the yield function $\mathbf{L} = \partial f / \partial \boldsymbol{\sigma}$ and the plastic flow direction $\mathbf{m}$ in stress space are given by

$$\mathbf{L} = \mathbf{n} - \frac{1}{3} N \mathbf{1} \tag{7}$$

$$\mathbf{m} = \mathbf{n} + \frac{1}{3} D \mathbf{1} \tag{8}$$

where

$$\mathbf{n} = \frac{\mathbf{r}}{\|\mathbf{r}\|} \tag{9}$$

$$N = \boldsymbol{\alpha} : \mathbf{n} + \sqrt{\frac{2}{3}} m \tag{10}$$

D = dilatancy coefficient

$\mathbf{1}$ = 2nd order identity tensor

and $\mathbf{n}$ represents the unit deviatoric stress-ratio tensor, i.e., $\mathbf{n} : \mathbf{n} = 1$ and $\text{tr}(\mathbf{n}) = 0$. While $\mathbf{L}$ denotes the normal to the yield surface (Eqn. 7), $\mathbf{m}$ defines the direction of plastic strain (Eqn. 8). The common component $\mathbf{n}$ in Eqns. 7 and 8 indicates that an associative flow rule is used in a deviatoric stress-ratio space. In contrast, the volumetric part of the flow rule is not associative, since in general $-N = D$. The evolution of plastic strains, $\dot{\boldsymbol{\varepsilon}}^p$, referred as "flow rule" is defined by

$$\dot{\boldsymbol{\varepsilon}}^p = \gamma\,\mathbf{m} \tag{11}$$

Where $\gamma \geq 0$ is a nonnegative parameter, here referred as the consistency parameter.

2.2 Critical, Dilatancy, and Bounding Surfaces in 3 − D Stress Space

The critical, dilatancy, and bounding surfaces are described in a general 3 −D space using Lode angle θ as shown in Fig. 1. Lode angle θ can be defined in terms of deviatoric stress invariants. That is,

$$\cos 3\theta = \frac{3\sqrt{3}}{2}\frac{J_3}{J_2^{3/2}} \tag{12}$$

where, J_2 and J_3 are the second and third invariants of the deviatoric stress tensor $\bar{\mathbf{r}} = \frac{\mathbf{r}}{p}$. With the help of Lode angle the functions for the surfaces can be generalized in a 3-dimensional space by means of a function g(θ, c) proposed by Willam and Warnke (Chen 1994) in which

$$g(\theta,c) = \frac{2(1-c^2)\cos(\theta-\pi/3) - (1-2c)\sqrt{4(1-c^2)\cos^2(\theta-\pi/3) + 5c^2 - 4c}}{4(1-c^2)\cos^2(\theta-\pi/3) + (1-2c)^2} \tag{13}$$

where c controls the shape of the bounding, critical, and dilation surfaces in the deviatoric space.

The locus of the bounding and dilatancy surfaces continuously change with the value of the state parameter, ψ, while the critical surface remains fixed. Their analytical description is obtained by three so-called "image" back-stress ratio tensors, $\boldsymbol{\alpha}_\theta^b$, $\boldsymbol{\alpha}_\theta^c$, and $\boldsymbol{\alpha}_\theta^d$, where superscripts b, c, and d represent the values associated with bounding, critical, and dilatancy surfaces, respectively, and θ indicates their dependence on Lode angle.

$$\boldsymbol{\alpha}_\theta^a = \sqrt{\frac{2}{3}}\alpha_\theta^a \mathbf{n}, \qquad (a = b,c,d) \tag{14}$$

Because $\mathbf{n}$ is defined from the given stress state, it remains to obtain the scalar-valued α_θ^a (notice the difference between the tensor-valued $\boldsymbol{\alpha}_\theta^a$ of the left-hand side and the scalar-valued α_θ^a of the right-hand side in Eqn. 14). Now, with the help of the state variable ψ and m, α_θ^a is defined as

$$\alpha_\theta^b = g(\theta,c)M_c + g(\theta,c_b)k_c^b\langle\psi\rangle - m \tag{15}$$

$$\alpha_\theta^d = g(\theta,c)M_c + g(\theta,c_d)k_c^d\psi - m \tag{16}$$

$$\alpha_\theta^c = g(\theta,c)M_c - m \tag{17}$$

where,

$$c = M_e/M_c, \quad c_b = k_e^b/k_c^b, \quad c_d = k_e^d/k_c^d \tag{18}$$

and Macauley bracket $\langle\ \rangle$ defines the operation $\langle\psi\rangle = \psi$ if $\psi > 0$ and $\psi = 0$ if $\psi \leq 0$. In above equations M_c is the critical state stress ratio and k_c^b and k_c^d are model surface parameters in compression side. The values with subscript e define the surface parameters in extension side. Eqns. 15~18 fully specify the bounding, dilatancy, and critical surfaces associated with the back-stress ratio α in a stress-ratio space.

2.3 Isotropic Hardening

The opening of the wedge like yield function depends on the hardening parameter m. The evolution of m can be expressed by

$$\dot{m} = \gamma\, c_m(1+e_0)D = \gamma\,\overline{m} \tag{19}$$

where c_m is a positive material parameter and e_0 is an initial void ratio.

2.4 Kinematic Hardening

The evolution of the back-stress ratio α is assumed to be dependent on the distance between the bounding back stress ratio and current back stress ratio, i.e., $\mathbf{b} = \boldsymbol{\alpha}_\theta^b - \boldsymbol{\alpha}$. Hence, the evolution of the kinematic hardening is given by

$$\dot{\boldsymbol{\alpha}} = \gamma\, h(\boldsymbol{\alpha}_\theta^b - \boldsymbol{\alpha}) = \gamma\,\overline{\boldsymbol{\alpha}} \tag{20}$$

where h is a positive scalar-valued function. The dependence of $\dot{\alpha}$ on the distance between α and $\boldsymbol{\alpha}_\theta^b$ satisfies

the bounding surface plasticity concept in that the plastic evolution is associated with such distance. The function h is adopted from the original work by Dafalias and Herrmann (1986). That is,

$$h = h_0 \frac{|\mathbf{b}:\mathbf{n}|}{b_{ref} - |\mathbf{b}:\mathbf{n}|} \tag{21}$$

where h_0 is a positive constant and b_{ref} is a reference scalar distance given by

$$b_{ref} = 2\sqrt{\frac{2}{3}}\alpha_\theta^b \tag{22}$$

Basically, Eqn. 22 denotes the diameter of the bounding surface.

2.5 Dilatancy Coefficient D

Based on Rowe's stress-dilatancy theory and its invariant form suggested by Nova and Wood (1979), it is assumed that the dilatancy coefficient D is proportional to the difference between the dilatancy back stress ratio and current back stress ratio, i.e., $\mathbf{d} = \boldsymbol{\alpha}_\theta^d - \boldsymbol{\alpha}$ such as

$$D = A(\alpha_\theta^d - \alpha):\mathbf{n} = A\mathbf{d}:\mathbf{n} \tag{23}$$

where A is a state dependent coefficient associated with an evolution of fabric formation.

2.6 Fabric Tensor F

In order to account for the effect of fabric formation on the unloading response, it is assumed that the variation of A in Eqn. 23 depends on an evolving fabric tensor F. That is,

$$A = A_0(1 + \langle \mathbf{F}:\mathbf{n} \rangle) \tag{24}$$

where A_0 is a positive constant. The evolution of the fabric tensor, $\dot{\mathbf{F}}$, is related to dilatancy and its effect is manifested by an increase in the dilatancy parameter A upon loading reversal (i.e., $\mathbf{F}:\mathbf{n} > 0$) enhancing a contractive response (Dafalias and Manzari 1999). In this study, the evolution of $\mathbf{F}$ is related only to accumulated plastic dilation. That is,

$$\dot{\mathbf{F}} = -\langle \gamma \rangle C_f \langle -D \rangle (F_{\max}\mathbf{n} + \mathbf{F}) \tag{25}$$

where the positive material constants C_f and $F_{\max}$ control the rate of change and maximum value of fabric tensor, respectively. The Macauley bracket defines the operation $\langle -D \rangle = -D$ if $-D > 0$ and $\langle -D \rangle = 0$ if $-D \le 0$.

2.7 Hypoelasticity

Using the fact that an elastic stress-strain relation can be decoupled into deviatoric (distortional) and volumetric parts, Hooke's law can be expressed in terms of deviatoric and volumetric strains. This leads to the following relations:

$$\dot{\mathbf{e}}^e = \frac{\dot{\mathbf{s}}}{2G} \tag{26}$$

$$\dot{\varepsilon}_v^e = \frac{tr(\dot{\boldsymbol{\sigma}})}{3K} \tag{27}$$

where $\dot{\mathbf{e}}^e$ and $\dot{\varepsilon}_v^e$ are the deviatoric and volumetric elastic strain increments, respectively, and G and K are shear and bulk modulus. Several researchers have studied the nonlinear characteristics of the parameters K and G. Hardin and Drenevich (1972) showed that there are three important parameters which affect the shear modulus: strain amplitude, effective mean principal stress, and void ratio. Thus, the shear modulus may be expressed by

$$G = G_0\left(\frac{p}{p_{atm}}\right)^b \tag{28}$$

where p_{atm} is the atmospheric pressure, b is a material constant, and G_0 is a reference shear modulus for $p = p_{atm}$. The bulk modulus, K, is not independent of G. For the case of isotropic linear elastic material, it can be related to G using Poisson's ratio, ν, as $K = \frac{2(1+\nu)}{3(1-2\nu)}G$.

2.8 The critical state line

The critical state line for this model is given by a straight line in $e-\ln p$ space. That is,

$$e_{cs} = e_{cs,ref} - \lambda \ln \frac{p}{p_{ref}} \tag{29}$$

where e_{cs} is the critical void ratio corresponding to mean effective stress p, $e_{cs,ref}$ is the reference critical void ratio at p_{ref}, and λ is the slope of $e-\ln p$ curve.

3. A Implicit Integration of the Two-surface Soil Plasticity Model

In this section, the equations that characterize the elastoplastic model described in the previous section are integrated using a implicit integration technique, specifically the CPPM method. This section follows the early work published by Manzari and Prachathananukit (2001), but the resulting non-linear system of equations is different from that proposed in Manzari and Prachathananukit (2001) in that the current work reduces the size of the system of equations by recognizing the dependence between stress and strain quantities. In what follows, the CPPM model specific procedure is presented.

3.1 Model Discretization

Using the notion of the implicit backward Euler method, the evolution laws are discretized for elastic strain ε^e, plastic internal variables α and m, and fabric tensor $\mathbf{F}$.

$$\boldsymbol{\varepsilon}^e = \boldsymbol{\varepsilon}^e_n + \Delta\boldsymbol{\varepsilon} - \Delta\gamma\, \mathbf{m}(\boldsymbol{\sigma},\boldsymbol{\alpha},m) \tag{30}$$

$$\boldsymbol{\alpha} = \boldsymbol{\alpha}_n + \Delta\gamma\, \overline{\boldsymbol{\alpha}} \tag{31}$$

$$m = m_n + \Delta\gamma\, \overline{m} \tag{32}$$

$$\mathbf{F} = \mathbf{F}_n - \Delta\gamma\, \overline{\mathbf{F}} \tag{33}$$

where $\mathbf{m} = \mathbf{n}_{n+1} + \frac{1}{3} D_{n+1}\mathbf{1}$ (Eqn. 30), $\overline{\boldsymbol{\alpha}} = h_{n+1}\mathbf{b}_{n+1}$ (Eqn. 31), $\overline{m} = c_m(1+e_0)D_{n+1}$(Eqn. 32), and $\overline{\mathbf{F}} = C_f\langle -D_{n+1}\rangle(F_{\max}\mathbf{n}_{n+1} + \mathbf{F})$ (Eqn. 33). It is implied in these equations that $\boldsymbol{\varepsilon}^e = \boldsymbol{\varepsilon}^e_{n+1}$, $\boldsymbol{\alpha} = \boldsymbol{\alpha}_{n+1}$, $m = m_{n+1}$, and $\mathbf{F} = \mathbf{F}_{n+1}$. The discrete form of the Kuhn-Tucker conditions is defined as

$$f(\boldsymbol{\sigma},\boldsymbol{\alpha},m,\mathbf{F}) \le 0 \tag{34}$$

$$\Delta\gamma \ge 0 \tag{35}$$

and the consistency condition results in

$$\Delta\gamma\, f(\boldsymbol{\sigma},\boldsymbol{\alpha},m,\mathbf{F}) \le 0 \tag{36}$$

3.2 Operator Split

Many implicit integration algorithms use an elastic-predictor plastic-corrector operator splitting approach (Oritz and Simo 1986), where a purely elastic trial (predictor) step is followed by a plastic (corrector) step. During the elastic predictor phase an approximate updated stress/strain for a given time/load step is assumed to be fully elastic. During the plastic corrector phase consistency is enforced at the end of the time step in a manner consistent with the discretized forms of the rate equations of plasticity (Simo and Hughes 1998). In the following discussion, the model is implemented based on the concept of operator splitting.

Elastic predictor

The first estimate of the updated state of stress and plastic internal variables is assumed to be the trial state defined as

$$\Delta\gamma^{trial} = 0 \tag{37}$$

$$\boldsymbol{\varepsilon}^{e^{trial}} = \boldsymbol{\varepsilon}_n + \Delta\boldsymbol{\varepsilon} \tag{38}$$

$$\boldsymbol{\sigma}^{trial} = \mathbf{C}^{trial} : \boldsymbol{\varepsilon}^{e^{trial}} \tag{39}$$

$$\boldsymbol{\alpha}^{trial} = \boldsymbol{\alpha}_n \tag{40}$$

$$m^{trial} = m_n \tag{41}$$

$$\mathbf{F}^{trial} = \mathbf{F}_n \tag{42}$$

$$f^{trial} = f\left(\boldsymbol{\sigma}^{trial}, \boldsymbol{\alpha}^{trial}, m^{trial}, \mathbf{F}^{trial}\right) \tag{43}$$

The trial elastic modulus tensor $\mathbf{C}^{trial}$ is obtained using the hypoelasticity. That is,

$$p^{trial} = \left[p_n^{(1-b)} + \frac{K_0(1-b)}{p^b{}_{atm}} tr(\Delta\boldsymbol{\varepsilon}^e) \right]^{\frac{1}{1-b}} \tag{44}$$

$$K^{trial} = \frac{p^{trial} - p_n}{tr(\Delta\boldsymbol{\varepsilon})} \tag{45}$$

$$G^{trial} = \frac{3}{2}\frac{(1-2\nu)}{(1+\nu)} K^{trial} \tag{46}$$

where b is a material constant. In case $\Delta\boldsymbol{\varepsilon} \to 0, K \to \frac{K_0}{p^b{}_{atm}} p^b{}_n$.

Plastic corrector

If $f(\boldsymbol{\sigma}^{trial}, \boldsymbol{\alpha}^{trial}, m^{trial}, \mathbf{F}^{trial}) > 0$, the plastic corrector step is triggered by enforcing the discretized Kuhn-Tucker conditions (Eqns. 34 and 35) and consistency requirement (Eqn. 36) together with the flow and hardening rules. For the Manzari-Dafalias model these equations are given in discrete form by Eqns. 30~33. In compact form these equations can be represented by an array of generalized residuals **R** and an array of generalized unknowns δ. That is,

$$\mathbf{R} = \begin{Bmatrix} \mathbf{R}_1 \\ \mathbf{R}_2 \\ R_3 \\ \mathbf{R}_4 \\ R_5 \end{Bmatrix} = \begin{Bmatrix} \boldsymbol{\varepsilon}^e - \boldsymbol{\varepsilon}_n^e - \Delta\boldsymbol{\varepsilon} + \Delta\gamma\mathbf{m} \\ \boldsymbol{\alpha} - \boldsymbol{\alpha}_n - \Delta\gamma\bar{\boldsymbol{\alpha}} \\ m - m_n - \Delta\gamma\bar{m} \\ \mathbf{F} - \mathbf{F}_n + \Delta\gamma\bar{\mathbf{F}} \\ \|\mathbf{r}\| - \sqrt{\frac{2}{3}} mp \end{Bmatrix}, \quad \boldsymbol{\delta} = \begin{Bmatrix} \boldsymbol{\delta}_1 \\ \boldsymbol{\delta}_2 \\ \delta_3 \\ \boldsymbol{\delta}_4 \\ \delta_5 \end{Bmatrix} = \begin{Bmatrix} \boldsymbol{\varepsilon}^e \\ \boldsymbol{\alpha} \\ m \\ \mathbf{F} \\ \Delta\gamma \end{Bmatrix} \tag{47}$$

The elements, $\mathbf{R}_1$, $\mathbf{R}_2$, $\mathbf{R}_4$, $\boldsymbol{\delta}_1$, $\boldsymbol{\delta}_2$, and $\boldsymbol{\delta}_4$ in the arrays **R** and δ respectively are symmetric 2nd order tensors. R_3, R_5, δ_3, and δ_5 are scalars. Setting **R** = **0** produces a system of twenty nonlinear equations and twenty unknowns representing the elastic strain, plastic internal variables, and consistency parameters. This also includes the algebraic evaluation of the variables

$$D = A(\mathbf{d} : \mathbf{n}) \tag{48}$$

$$A = A_0\left(1 + \langle \mathbf{F} : \mathbf{n} \rangle\right) \tag{49}$$

$$h = h_0 \frac{|\mathbf{b} : \mathbf{n}|}{b_{ref} - |\mathbf{b} : \mathbf{n}|} \tag{50}$$

$$b_{ref} = 2\sqrt{\frac{2}{3}}\alpha_\theta^b \tag{51}$$

$$\mathbf{b} = \sqrt{\frac{2}{3}}\alpha_\theta^b \mathbf{n} - \boldsymbol{\alpha} \tag{52}$$

$$\mathbf{d} = \sqrt{\frac{2}{3}}\alpha_\theta^d \mathbf{n} - \boldsymbol{\alpha} \tag{53}$$

Stress update algorithm

By setting $\mathbf{R} = 0$ in Eqn. 47, the unknowns are obtained effectively by using a Newton's iterative algorithm. The method consists of iterating over the expressions

$$k \leftarrow k+1, \quad -\mathbf{J}^k \Delta\boldsymbol{\delta}^k = \mathbf{R}, \quad \boldsymbol{\delta}^{k+1} = \boldsymbol{\delta}^k + \Delta\boldsymbol{\delta}^k \tag{54}$$

where $J^k = \frac{\partial \mathbf{R}^k}{\partial \boldsymbol{\delta}^k}$ is the consistent Jacobian which, in this case, takes the explicit form of

$$\mathbf{J}^k = \begin{bmatrix} \mathbf{I} + \Delta\gamma\frac{\partial \mathbf{m}}{\partial \boldsymbol{\varepsilon}^e} & \Delta\gamma\frac{\partial \mathbf{m}}{\partial \boldsymbol{\alpha}} & \Delta\gamma\frac{\partial \mathbf{m}}{\partial m} & \Delta\frac{\partial \mathbf{m}}{\partial \mathbf{F}} & \mathbf{m} \\ -\Delta\gamma\frac{\partial \bar{\boldsymbol{\alpha}}}{\partial \boldsymbol{\varepsilon}^e} & \mathbf{I} - \Delta\gamma\frac{\partial \bar{\boldsymbol{\alpha}}}{\partial \boldsymbol{\alpha}} & -\Delta\gamma\frac{\partial \bar{\boldsymbol{\alpha}}}{\partial m} & \mathbf{0} & -\bar{\boldsymbol{\alpha}} \\ -\Delta\gamma\frac{\partial \bar{m}}{\partial \boldsymbol{\varepsilon}^e} & -\Delta\gamma\frac{\partial \bar{m}}{\partial \boldsymbol{\alpha}} & 1 - \Delta\gamma\frac{\partial \bar{m}}{\partial m} & -\Delta\gamma\frac{\partial \bar{m}}{\partial \mathbf{F}} & -\bar{m} \\ \Delta\gamma\frac{\partial \bar{\mathbf{F}}}{\partial \boldsymbol{\varepsilon}^e} & \Delta\gamma\frac{\partial \bar{\mathbf{F}}}{\partial \boldsymbol{\alpha}} & \Delta\gamma\frac{\partial \bar{\mathbf{F}}}{\partial m} & \mathbf{I} + \Delta\gamma\frac{\partial \bar{\mathbf{F}}}{\partial \mathbf{F}} & \bar{\mathbf{F}} \\ 2G\mathbf{n} - K\left(\sqrt{\frac{2}{3}}m + \boldsymbol{\alpha} : \mathbf{n}\right)\mathbf{1} & -p\mathbf{n} & -\sqrt{\frac{2}{3}}p & \mathbf{0} & 0 \end{bmatrix} \tag{55}$$

During the iteration procedure the elastic modulus **C** is updated using the hypoelastic relations given by

$$p^{trial} = \left[p_n^{(1-b)} + \frac{K_0(1-b)}{p^b{}_{atm}} \left[tr(\Delta\boldsymbol{\varepsilon}^e) - tr(\Delta\boldsymbol{\varepsilon}_n^e) \right] \right]^{\frac{1}{1-b}} \tag{56}$$

$$K^{trial} = \frac{p^{trial} - p_n}{tr(\Delta\boldsymbol{\varepsilon}) - tr(\Delta\boldsymbol{\varepsilon}_n^e)} \tag{57}$$

The iteration procedure is considered to have converged to a solution when $\|\mathbf{R}\| < Tol$, where *Tol* is an acceptable residual norm error. Table 2 describes the step by step stress update algorithm.

3.3 Consistent Tangent Operator

In a finite element framework the stress update algorithm presented above is performed at each Gauss quadrature point. At the global finite element level, a nonlinear system of equations needs to be solved to satisfy the balance of momentum (equilibrium). Various nonlinear solvers are available for this purpose (Dennis and

Table 2. Closest-Point-Projection iteration for the Manzari-Dafalias two-surface soil plasticity model

1. Initialize: $k=0,\ \boldsymbol{\varepsilon}^{e^{(0)}}=\boldsymbol{\varepsilon}_n+\Delta\boldsymbol{\varepsilon},\ \boldsymbol{\alpha}^{(0)}=\boldsymbol{\alpha}_n,\ m^{(0)}=m_n,\ \mathbf{F}^{(0)}=\mathbf{F}_n,\ \Delta\gamma^{(0)}=0$

2. Get trial stress, check yield condition, and evaluate the residuals

$\mathbf{C}^{(k)}=f(\boldsymbol{\sigma}_n,\Delta\boldsymbol{\varepsilon}^e)$ *(Eqns. 45 and 46)*

$\boldsymbol{\sigma}^{(k)}=\boldsymbol{\sigma}_n+\mathbf{C}:\left(\boldsymbol{\varepsilon}^{e^{(k)}}-\boldsymbol{\varepsilon}_n^e\right)$

$f_{n+1}^{(k)}=f\left(\boldsymbol{\sigma}^{(k)},\boldsymbol{\alpha}^{(k)},m^{(k)}\right)$ **note* $f=$ *yield function*

$$\mathbf{R}^{(k)}=\begin{Bmatrix}\boldsymbol{\varepsilon}^{e^{(k)}}-\boldsymbol{\varepsilon}_n^e-\Delta\boldsymbol{\varepsilon}+\Delta\gamma^{(k)}\mathbf{m}^{(k)}\\ \boldsymbol{\alpha}^{(k)}-\boldsymbol{\alpha}_n-\Delta\gamma^{(k)}\overline{\boldsymbol{\alpha}}^{(k)}\\ m^{(k)}-m_n-\Delta\gamma^{(k)}\overline{m}^{(k)}\\ \mathbf{F}^{(k)}-\mathbf{F}_n+\Delta\gamma^{(k)}\overline{\mathbf{F}}^{(k)}\\ \left\|\mathbf{r}^{(k)}\right\|-\sqrt{\frac{2}{3}}m^{(k)}p^{(k)}\end{Bmatrix}$$

If $f_{n+1}^{(k)}<Tol_1$ and $\|R\|<Tol_2$ then: Exit

3. Linearize the residual and obtain increments of variables

$$\mathbf{J}^{(k)}=\frac{\partial\mathbf{R}^{(k)}}{\partial\left(\boldsymbol{\varepsilon}^{e(k)},\boldsymbol{\alpha}^{(k)},m^{(k)},\mathbf{F}^{(k)},\Delta\gamma^{(k)}\right)}$$

$$\Delta\left[\boldsymbol{\varepsilon}^{e(k)},\boldsymbol{\alpha}^{(k)},m^{(k)},\mathbf{F}^{(k)},\Delta\gamma^{(k)}\right]=-\mathbf{J}^{(k)^{-1}}\mathbf{R}^{(k)}$$

4. Update state variables and consistency parameter

$\boldsymbol{\varepsilon}^{e^{(k+1)}}=\boldsymbol{\varepsilon}^{e^{(k)}}+\Delta\boldsymbol{\varepsilon}^{e^{(k)}}$

$\boldsymbol{\alpha}^{(k+1)}=\boldsymbol{\alpha}^{(k)}+\Delta\boldsymbol{\alpha}^{(k)}$

$m^{(k+1)}=m^{(k)}+\Delta m^{(k)}$

$\mathbf{F}^{(k+1)}=\mathbf{F}^{(k)}-\Delta\mathbf{F}^{(k)}$

$\Delta\gamma^{(k+1)}=\Delta\gamma^{(k)}+\Delta^2\gamma^{(k)}$

Set $k\leftarrow k+1$ and GOTO 2

Schnabel 1996), but one of the most common choices is Newton's method. It is well known that the use of the consistent tangent operator $\frac{d\boldsymbol{\sigma}}{d\boldsymbol{\varepsilon}}$, which is the discretized algorithmic version of the elastoplastic tangent moduli (or continuum tangent), preserves the asymptotic rate of quadratic convergence of the global iterative process (Simo and Taylor 1985). The fact that the evolution equations can be exactly linearized using the CPPM in explicit form (Eqn. 55) leads to an important numerical strategy that can lead to an efficient global iterative scheme.

For a given strain increment, as $\mathbf{R}\rightarrow 0$, the residual equations in Eqn. 47 are rewritten as

$$\boldsymbol{\varepsilon}^e+\Delta\gamma\, m(\boldsymbol{\sigma},\boldsymbol{\alpha},m,\mathbf{F})=\boldsymbol{\varepsilon}_n^e+\Delta\boldsymbol{\varepsilon} \tag{58}$$

$$\boldsymbol{\alpha}-\Delta\gamma\,\overline{\boldsymbol{\alpha}}(\boldsymbol{\sigma},\boldsymbol{\alpha},m)=\boldsymbol{\alpha}_n \tag{59}$$

$$m-\Delta\gamma\,\overline{m}(\boldsymbol{\sigma},\boldsymbol{\alpha},m,\mathbf{F})=m_n \tag{60}$$

$$\mathbf{F}+\Delta\gamma\,\overline{\mathbf{F}}(\boldsymbol{\sigma},\boldsymbol{\alpha},m,\mathbf{F})=\mathbf{F}_n \tag{61}$$

$$f(\boldsymbol{\sigma},\boldsymbol{\alpha},m)=0 \tag{62}$$

and after linearization they take the explicit compact form,

$$\mathbf{J}\begin{Bmatrix}d\boldsymbol{\varepsilon}^e\\ d\boldsymbol{\alpha}\\ dm\\ d\mathbf{F}\\ d\Delta\gamma\end{Bmatrix}=\begin{Bmatrix}d\boldsymbol{\varepsilon}\\ \mathbf{0}\\ 0\\ \mathbf{0}\\ 0\end{Bmatrix}\quad or\quad \begin{Bmatrix}d\boldsymbol{\varepsilon}^e\\ d\boldsymbol{\alpha}\\ dm\\ d\mathbf{F}\\ d\Delta\gamma\end{Bmatrix}=\mathbf{J}^{-1}\begin{Bmatrix}d\boldsymbol{\varepsilon}\\ \mathbf{0}\\ 0\\ \mathbf{0}\\ 0\end{Bmatrix} \tag{63}$$

The first element of this array holds information related to the consistent tangent moduli. By extraction of the upper-left block of the Jacobian matrix it is possible to get

$$d\boldsymbol{\varepsilon}^e = \mathbf{P}^T \mathbf{J}^{-1} \mathbf{P} d\boldsymbol{\varepsilon} \tag{64}$$

where $\mathbf{P}^T = \left(\mathbf{I}_{\dim(\varepsilon)}, \mathbf{0}_{\dim(\alpha)+\dim(m)+\dim(F)+1}\right)$ is a projection matrix. The Cauchy stress tensor is then obtained using Hooke's law

$$d\boldsymbol{\sigma} = \mathbf{P}^T \mathbf{J}^{-1} \mathbf{P} \mathbf{C} : d\boldsymbol{\varepsilon} \tag{65}$$

Then, the elastoplastic consistent tangent moduli takes the explicit form (Perez-Foguet et al. 2000a; Perez-Foguet et al. 2000b) of

$$\mathbf{C}^{ep} = \mathbf{P}^T \mathbf{J}^{-1} \mathbf{P} \mathbf{C} \tag{66}$$

4. Asscessment of the Performance of CPPM Scheme

In this section, the robustness, accuracy, and efficiency of the numerical algorithm used in this study are evaluated. For this purpose (1) model simulations of stress-strain behavior for coarse-grained soils subjected to realistic stress paths encountered in soil testing are presented. Model parameters are obtained in the course of calibrating coarse-grained soils as proposed by Choi (2004), (2) an isoerror map is constructed to assess stress errors generated by different strain increments, and (3) the convergence rate of the global iteration process is evaluated using the consistent tangent operator, $\mathbf{C}^{ep}$, and the tensor of elastic moduli, $\mathbf{C}$.

Because most finite element aprroxiamtions postulate the constitutive equations in terms of strains, the integration algorithms are formulated as strain-driven algorithms. However, it is important to have a mixed formulation to simulate soil laboratory testing, because, in general, driven varables during lab-testing consist of the mixture between stress and strain. In order to implement a mixed control driver, together with an incremental constitutive law formulation, iterative procedures are needed that aim at satisfying the equilibrium of updated stresses with respect to prescribed stress components. This step is similar to what is commonly done in finite element analysis during a global equilibrium iterative step. In the following simulations a 'Mixed-control driver' was used based on the work done by Alawaji (1990) and Alawaji and Runesson (1991).

4.1 Model Simulations Subjected to Typical Stress-paths

Using the model parameters referred to as Set 1 in Table 3 and p_0 = 160 kPa, Fig. 3 shows the model response subjected to strain-controlled conventional triaxial compression loading. The results are presented in terms of q vs. p, q vs. ε_s, and Δu vs. ε_s plots. The initial void ratio, i.e., e_0 = 0.623, was used in the simulations. Tolerances shown in Table 2, Tol_1 = 0.000001 and Tol_2 = 0.000001, are set for integration algorithm. Three specimens are loaded to reach a maximum vertical strain of 0.1 (10%). The figure shows the performance of three simulations with the vertical strain increments of 0.005, 0.002, and 0.0002. The simulation with a strain increment of 0.0002 is

Table 3. Model parameters used for simulation

Elastic parameters	Set 1	Set 2
K_0	32400 kPa	31400 kPa
ν	0.25	0.2
b	0.86	0.5
Critical state Parameters		
M_c / M_e	1.62/1.13	1.30/1.14
λ	0.018	0.025
$e_{cs,ref}$	0.590	0.8
p_{ref}	1020 kPa	160 kPa
Model parameters		
k_c^b / k_e^b	4.3/2.3	4.0/2.0
k_c^d / k_e^d	27.6/15.2	4.2/0.07
h_0	1500	1200
c_m	0.0	0.0
m	0.05	0.05
A_0	0.50	2.64
$F_{\max}$	100	100
C_f	100	100

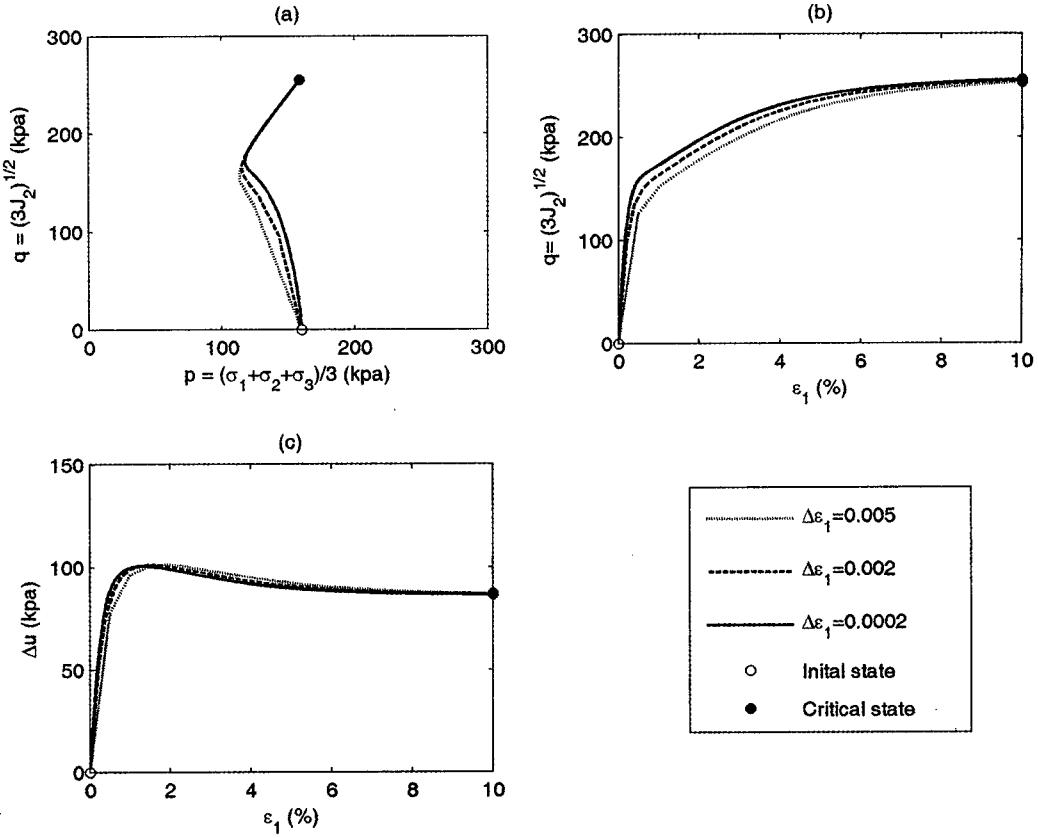

Fig. 3. Model simulation using closest-point-projection method with varying strain increment magnitudes under conventional triaxial-compression loading: (a) stress path, (b) axial strain vs. deviatoric stress, and (c) pore water pressure vs. axial strain.

assumed to be exact results. As shown in the figure all simulations are very close to each other indicating the accuracy of the integration scheme in a relatively broad range of strain increments. It is also noted that the integration algorithm well accomodates the nonlinear strain-hardening/softening behavior.

An error of estimated stresses was evaluated between the simulation of 0.005 and 0.002. Here, a relative error, ERR, is estimated using the expression

$$ERR = \frac{\sqrt{(\sigma - \sigma^*) : (\sigma - \sigma^*)}}{\sqrt{\sigma : \sigma^*}} \qquad (67)$$

where σ is a stress state obtained from the algorithm and σ* is the exact solution corresponding to a specified strain increment. Figure 4 shows a relative error of estimated stresses where the exact solution was assumed to be the simulation of 0.005 increment. The relative error was initially high and decreases as the state of stress gets closer to the critical state.

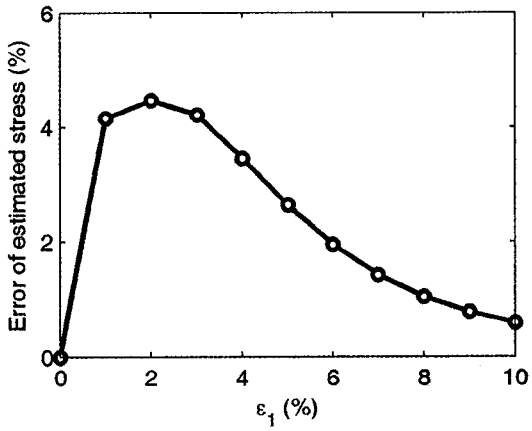

Fig. 4. Comparison of the errors in estimated stresses obtained using $\Delta\varepsilon_1 = 0.5\%$ and $\Delta\varepsilon_1 = 0.2\%$ for strain-controlled conventional triaxial compression loading.

As a second test the performance of the Manzari-Dafalias Model together with the integration algorithm is shown in Fig. 5 which depicts a model simulation under pure shear loading. An applied incremental strain tensor is given by

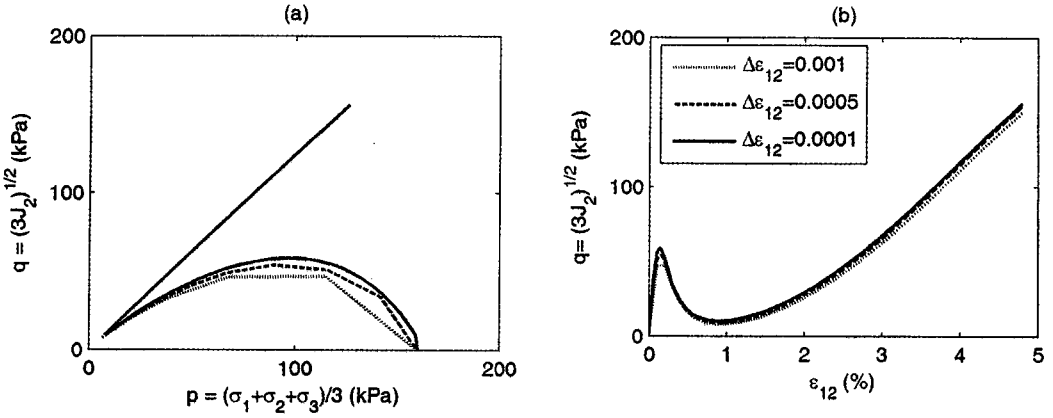

Fig. 5. Model simulation with varying shear strain increment magnitudes under pure shear strain loading: (a) stress path and (b) shear strain vs. shear stress

$$\Delta\boldsymbol{\varepsilon} = \begin{bmatrix} 0 & \Delta\varepsilon_{12} & 0 \\ \Delta\varepsilon_{12} & 0 & 0 \\ 0 & 0 & 0 \end{bmatrix} \tag{68}$$

Figures 5 (a) and 5 (b) show model responses in a q vs. p and q vs. ε_s with the shear strain increments, $\Delta\varepsilon_{12}$, of 0.002, 0.001, and 0.0002, respectively. The parameters of Set 2 in Table 2 and the initial void ratio, i.e., e_0 = 0.810, were used in the simulations. From the simulations, it is again concluded that all simulations are very close to each other and the accuracy of the integration scheme in a relatively broad range of strain increments is acceptable.

4.2 Accuracy Assessment of the CPPM Method : Isoerror Map

In order to assess the accuracy of the CPPM integration algorithm used in this study an isoerror map was constructed for selected stress states based on strain-controlled simulations using Eqn. 67. Similar procedures have been used for the same purpose by a number of authors (Ortiz and Popov 1985; Ortiz and Simo 1986; Macari, et al. 1997; Borja, et al. 2001; Manzari and Prachathananukit 2001). The exact solution σ* of Eqn. 67 for any given strain increment was obtained by dividing the desired strain increment into 500 steps with further subincrementation producing no significant change in the numerical results.

The parameters referred to as Set 1 in Table 3 were

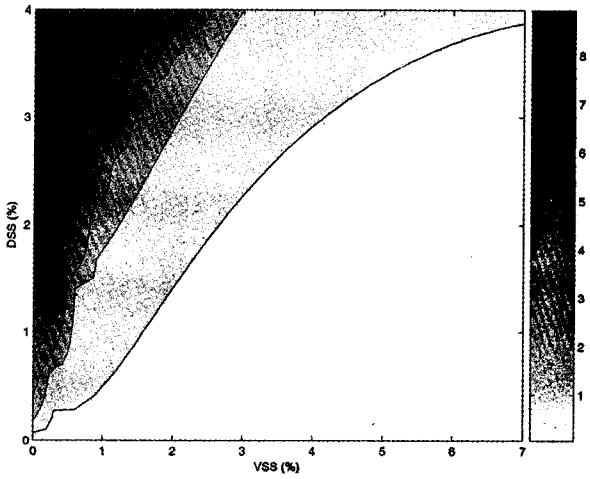

Fig. 6. Isoerror map for closest-point-projection method.

used for generating the isoerror map. An initial mean effective stress, p_0, of 69 kPa and a void ratio, e_0, of 0.610 were used in the simulations. To bring the state variables to a plastic state $\varepsilon_{11} = 0.05\%$ was first applied as an initial condition. The isoerror map was generated by applying linear combinations of isotropic compression and deviatoric shearing. Isotropic compression was defined by equal compressive strain increments (i.e., $\Delta\varepsilon_{11} = \Delta\varepsilon_{22} = \Delta\varepsilon_{33} > 0$) while holding all shear components (i.e., $\Delta\varepsilon_{12} = \Delta\varepsilon_{13} = \Delta\varepsilon_{23} = 0$). Deviatoric shearing was defined by equal shear strain increments (i.e., $\Delta\varepsilon_{12} = \Delta\varepsilon_{13} = \Delta\varepsilon_{23} > 0$) while holding all compressive components (i.e., $\Delta\varepsilon_{11} = \Delta\varepsilon_{22} = \Delta\varepsilon_{33} = 0$). The isoerror map was then plotted on a plane defined in terms of the volumetric step size ($VSS = \Delta\varepsilon_{11} + \Delta\varepsilon_{22} + \Delta\varepsilon_{33}$) and deviatoric step size ($DSS = \sqrt{2(\Delta\varepsilon_{12}^2 + \Delta\varepsilon_{13}^2 + \Delta\varepsilon_{23}^2)/3}$). Figure 6 shows an

isoerror map for the CPPM algorithm. Inspection of this figure shows that the order of the error increases as the strain increments become larger. Note that errors are more pronounced with increasing step size in the deviatoric shearing direction than in the volumetric compression direction. This is consistent with the fact that the current formulation does not account for plastic yielding during pure volumetric loading. Overall, the CPPM algorithm tends to be accurate even for large strain increments.

4.3 Accuracy Assessment of the CPPM Method : Convergence Rate

The main benefit of the CPPM integration algorithm is that the resulting constitutive rate equations can be exactly linearized (Simo and Hughes 1998). It is well known that the use of a linearized stiffness, or consistent tangent operator $\frac{d\sigma}{d\varepsilon}$, which is the discretized algorithmic version of the elastoplastic tangent moduli, preserves the asymptotic rate of quadratic convergence of global finite element Newton's iteration processes. Here, such a convergence rate is illustrated by means of a simple numerical example.

Using the model parameters referred to as Set 1 in Table 3 Fig. 7 shows convergence results for several load steps. In the simulation, an initial mean effective stress, p_0, of 69 kPa and an initial void ratio, e_0, of 0.60 were used. The convergence results shown in Figs. 7 (b), (c), and (d) were obtained for load steps "1", "2", and "3" as shown in Fig. 7 (a). The 'Mixed-control driver' developed in this study was used at the global iteration level. The figures show convergence rates for two different iteration moduli, i.e., tensor of elastic moduli, **C**, and consistent tangent operator, $\mathbf{C}^{ep}$, as plots of relative error $|\mathbf{g}|/|\mathbf{g}_0|$ vs. number of iterations; where "**g**" denotes a measure of the unbalanced equilibrium stress error. **C** is defined by the elastic moduli obtained at each load step in the first iteration, while $\mathbf{C}^{ep}$ is the consistent tangent operator evaluated for every CPPM iteration (Eqn. 66). It is clear that the number of global iteration steps required

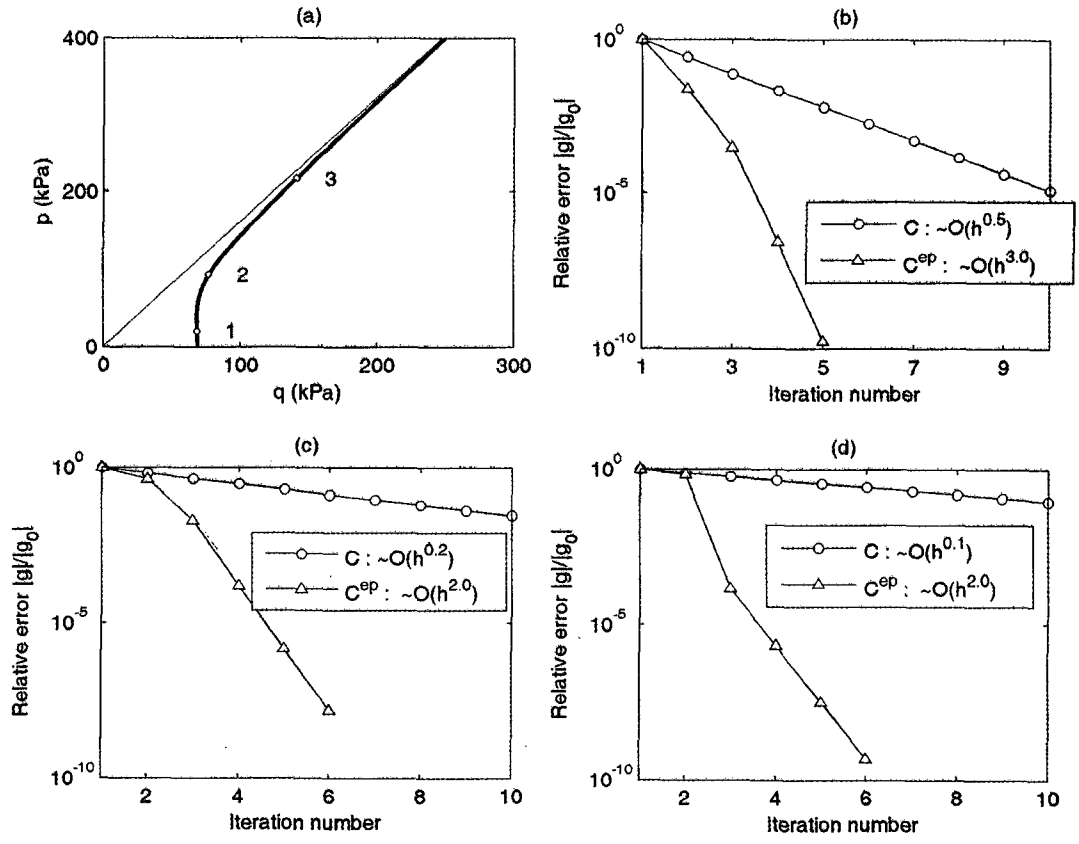

Fig. 7. Convergence results for mixed constitutive driver using $\mathbf{C}$ *and* $\mathbf{C}^{ep}$ *as global iteration matrices: (a) applied stress path, (b) convergence rate for stress point1, (c) convergence rate for stress point 2, and (d) convergence rate for stress point 3.*

for convergence using $\mathbf{C}^{ep}$ is much less than that required using $\mathbf{C}$. Moreover, it is observed that the order of convergence obtained using $\mathbf{C}^{ep}$ preserves a quadratic rate. It is also interesting to note that, when using $\mathbf{C}$, the convergence rate tends to depend on the state of stress, i.e., as the stress state gets closer to the critical state, the rate of convergence tends to decrease.

5. Conclusion

In this paper a numerical integration technique for two-surface soil plasticity was presented. An implicit Backward Euler method was selected because of its simplicity and robustness associated with numerical implementation of classical plasticity. It was shown that the use of the Backward Euler method leads to the notion of the Closest Point Projection Method (CPPM) as a generalized return mapping algorithm that uses operator splitting, that is, an elastic-predictor step followed by a plastic-corrector step. A discrete form of the Manzari-Dafalias soil plasticity model was presented within a CPPM formulation, including nonlinear kinematic and isotropic hardening. Finally, the consistent tangent operator $\frac{d\sigma}{d\varepsilon}$, which is the discretized algorithmic version of the elastoplastic tangent moduli, was obtained by extracting information from the Jacobian with an aid of a projection matrix.

In order to evaluate the robustness and accuracy of the CPPM algorithm, several model simulations under typical stress-paths were presented and an isoerror map was created for estimated stress states based on strain-controlled numerical simulations. The results showed that the CPPM algorithm produces robust and accurate estimate of stress, even for relatively large strain increments. To assess the efficiency of the CPPM method, the convergence rate of the global iteration process was evaluated. The results showed that using the consistent tangent operator a quadratic rate of convergence is achieved. Based on the verification studies, it is concluded that the CPPM algorithm used for the integration of the constitutive relations provides an accurate and robust numerical implementation.

Acknowledgement

This work was supported by the National Science Foundation (Grant No. CMS-0100518). The authors are grateful to Professor Pedro Arduino and Gregory Miller at the University of Washington for sharing his idea and valuable discussions on this work.

References

1. Alawaji, H. A. S. (1990), *Formulation and Integration of Constitutive Relations in Soil Plasticity Under Mixed Control for Drained and Undrained Conditions*, PhD Thesis, University of Colorado, Boulder.
2. Alawaji, H. A. S., and Runesson, K. (1991), "Intergation of constitutive equations in soil plasticity", *ASCE Journal of Engineering Mechanics*, Vol.117, No.8, pp.1771-1790.
3. Borja, R. I., and Lee, S. R. (1990), "Cam-clay plasticity, part I: Implicit integration of elasto-plastic constitutive relations", *Computer Method in Applied Mechanics and Engineering*, Vol.78, pp.49-72.
4. Borja, R. I. (1991), "Cam-clay plasticity, part II: Implicit integration of constitutive equation based on a nonlinear elastic stress predictor", *Computer Method in Applied Mechanics and Engineering*, Vol.88, pp.225-240.
5. Borja, R. I., Lin, C.-H., and Montans, F. J. (2001), "Cam-clay plasticity, part VI: Implicit integration of anisotropic bounding surface model with nonlinear hyperelasticity and ellipsoidal loading function", *Computer Method in Applied Mechanics and Engineering*, Vol.90, pp.3293-3323.
6. Chen, W. F. (1994), *Constitutive Equations for Engineering Materials*, Vol.2, Elsevier Science, Amsterdam.
7. Choi, C. H. (2004), *Physical and Mathematical Modeling of Coarse-Grained Soils*, PhD Thesis, University of Washington.
8. Dafalias, Y. F., and Herrmann, L. R. (1986), "Bounding surface plasticity II: Application to isotropic cohesive soils", *ASCE Journal of Engineering Mechanics*, Vol.112, No.12, pp.1263-1981.
9. Dafalias, Y. F., and Manzari, M. T. (1999), "Modeling of fabric effect on the cyclic loading response of granular soils", *Proc. Of the 13th ASCE Engineering Mechanics Conference*, Johns Hopkins University, Baltimore, USA.
10. Dennis, J. E., and Schnabel, R. B. (1996), *Numerical Methods for Unconstrained Optimization and Nonlinear Equations*, SIAM.
11. Hardin, B. O., and Drnevich, V. P. (1972), "Shear modulus and damping in soils: Measurement and parameter effects", *In Proceedings of ASCE*, Vol.98(SM6), pp.603-624.
12. Hashash, Y. M. A., and Whittle, A. J. (1992), "Integration of the modified camclay model in non-linear finite element analysis", *Computers and Geotechnics*, Vol.14, pp.59-83.
13. Jacobsson, L., and Runesson, K. (2002), "Intergation and calibration of a plasticity model for granular materials", *International Journal for Numerical and Analytical Methods in Geomechanics*, Vol.26, pp.259-272.
14. Jeremic, B., and Sture, S. (1997), "Implicit integrations in elasto-plastic geotechnics", *Mechanics of Cohesive-Frictional Materials*, Vol.2, pp.165-183.

15. Macari, E. J., Weihe, S., and Arduino, P. (1997), "Implicit integration of elastoplastic constitutive models for frictional materials with highly non-linear hardening functions", *Mechanics of Cohesive-Frictional Materials*, Vol.2, pp.1-29.
16. Manzari, M. T., and Dafalias, Y. F. (1997), "A critical state two-surface plasticity model for sands", *Geotechnique*, Vol.47, No.2, pp.255-272.
17. Manzari, M. T., and Prachathananukit, R. (2001), "On integration of a cyclic soil plasticity model", *International Journal for Numerical and Analytical Methods in Geomechanics*, Vol.25, No.6, pp.525-549.
18. Nova, R., and Wood, D. M. (1979), "A constitutive model for sand in triaxial compression", *International Journal for Numerical and Analytical Methods in Geomechanics*, Vol.3, pp.255-278.
19. Ortiz, M., Pinsky, P. M., and Taylor, R. L. (1983), "Operator split methods for the numerical solution of the elastoplastic dynamic problem", *Computer Methods in Applied Mechanics and Engineering*, Vol.39, pp.137-157.
20. Ortiz, M., and Popov, E. P. (1985), "Accuracy and stability of integration algorithms for elastoplastic constitutive relations", *International Journal for Numerical Methods in Engineering*, Vol.21, pp.1561-1576.
21. Ortiz, M., and Simo, J. C. (1986), "An analysis of a new class of integration algorithms for elastoplastic constitutive relations", *International Journal for Numerical Methods in Engineering*, Vol.23, pp.353-366.
22. Perez-Foguet, A., Rodriguez-Ferran, A., and Huerta, A. (2000a), "Numerical differentiation for local and global tangent operators in computational plasticity", *Computer Methods in Applied Mechanics and Engineering*, Vol.189, pp.277-296.
23. Perez-Foguet, A., Rodriguez-Ferran, A., and Huerta, A. (2000b), "Numerical differentiation for non-trivial consistent tangent matrices: An application to the MRS-Lade model", International Journal for Numerical Methods in Engineering, Vol.48, pp.159-184.
24. Simo, J. (1998), *Handbook of Numercial Analysis*, Vol.VI, pp. 179-499, Elsevier.
25. Simo, J. C., and Hughes, T. (1987), "General return mapping algorithms for rateindependent plasticity", *In Constitutive Laws for Engineering Materials, Theory and Applications*, C. Desai, Ed., Vol.1, pp.221-231.
26. Simo, J. C., and Hughes, T. J. R. (1998), *Computational Inelasticity, Springer*.
27. Simo, J. C., and Taylor, R. L. (1985), "Consistent tangent operators for rateindependent elastoplasticity", *Computer Methods in Applied Mechanics and Engineering*, Vol.48, pp.101-118.
28. Simo, J. C., and Taylor, R. (1986), "Return mapping algorithm for plane stress elastoplasticity", *International Journal for Numerical Methods in Engineering*, Vol.2200, pp.649-670.

(received on May 12, 2006, accepted on Sep. 4, 2006)